

# Gaussian conversion protocols for cubic phase state generation

Yu Zheng<sup>1</sup>, Oliver Hahn<sup>1</sup>, Pascal Stadler<sup>1</sup>, Patric Holmvall<sup>1</sup>, Fernando Quijandra<sup>1</sup>, Alessandro Ferraro<sup>2</sup> and Giulia Ferrini<sup>1</sup>

<sup>1</sup> Wallenberg Centre for Quantum Technology, Department of Microtechnology and Nanoscience, Chalmers University of Technology, Sweden

<sup>2</sup> Centre for Theoretical Atomic, Molecular and Optical Physics,  
Queen's University Belfast, Belfast BT7 1NN, United Kingdom \*

(Dated: July 8, 2020)

Universal quantum computing with continuous variables requires non-Gaussian resources, in addition to a Gaussian set of operations. A known resource enabling universal quantum computation is the cubic phase state, a non-Gaussian state whose experimental implementation has so far remained elusive. In this paper, we introduce two Gaussian conversion protocols that allow for the conversion of a non-Gaussian state that has been achieved experimentally, namely the trisqueezed state [Sandbo Chang *et al.*, Phys. Rev. X **10**, 011011 (2020)], to a cubic phase state. The first protocol is deterministic and it involves active (in-line) squeezing, achieving large fidelities that saturate the bound for deterministic Gaussian protocols. The second protocol is probabilistic and it involves an auxiliary squeezed state, thus removing the necessity of in-line squeezing but still maintaining significant success probabilities and fidelities even larger than for the deterministic case. The success of these protocols provides strong evidence for using trisqueezed states as resources for universal quantum computation.

## I. INTRODUCTION

Continuous-Variable (CV) systems [1] are promising candidates to implement quantum computation in a variety of physical settings where quantum systems cannot be described within a finite dimensional Hilbert space, including optical [2] and microwave radiation [3–5], trapped ions [6, 7], optomechanical systems [8–10], atomic ensembles [11–14], and hybrid systems [15]. A major feature of CV systems is their potential in terms of scalability and noise resilience. In the optical domain, dual-rail cluster states composed of up to one-million modes have been implemented [16], as well as large bi-dimensional cluster states [17, 18], with the potential of on-chip integrability [19]. In the microwave regime, the use of bosonic codes in superconducting cavities has allowed for extending the life-time of quantum information with respect to the constituents of the system [20], and recent architectures allow for a lifetime of photons in 3D-cavities of up to two seconds [21]. Furthermore, bosonic codes that render CV quantum computation fault-tolerant against arbitrary errors, namely Gottesman-Kitaev-Preskill (GKP) codes [22, 23], have also been recently experimentally achieved [24].

In CV quantum computation, Gaussian operations play a central role [25–27], given that in general they are relatively easy to implement regardless the chosen experimental platform. However, Gaussian operations alone cannot achieve computational universality [22, 28], and genuine quantum non-Gaussianity is required as a resource [29, 30]. In particular, two main routes have been identified in order to promote Gaussian operations to universality by means of resourceful states. The first one relies upon the states that embody the specific codewords of the already mentioned GKP code [22, 31, 32]. The second route is instead based on the so called cubic phase state [22] which, by enabling the implementation of a non-linear gate [33], can in principle unlock universality regardless the use of a specific encoding [28] —

including, for example, the GKP encoding via the probabilistic protocol introduced in Ref. [34].

Whereas GKP codeword states have recently been produced experimentally [24, 35], the generation of a cubic phase state has proven elusive thus far, despite the considerable theoretical [22, 36–40] as well as experimental [41] effort. The purpose of this work is to provide viable solutions for the generation of a cubic phase state, exploiting a family of non-Gaussian Wigner-negative states that have been recently generated experimentally.

As a matter of fact, a number of experiments have demonstrated the generation of non-Gaussian Wigner-negative states, both in the optical domain — typically using photon subtraction and addition operations [42–44] — and in the microwave domain — using controlled qubit-mediated operations [24, 45, 46] or other form of non-linearities [47–52]. However, it is not known currently which non-Gaussian states can be converted into resource states for quantum computation, such as the cubic phase state, by means of resourceless (Gaussian) protocols. In Ref. [29], a bound on the number of copies needed for the conversion, based on the ratio of the negativities of the Wigner function of the input and target state, has been derived. However, this bound is non-constructive, in the sense that even if the bound is satisfied, it is not guaranteed that a conversion protocol saturating the bound exists. In general, conversion protocols that yield as an output state a resource state starting from experimentally accessible states have not been studied thoroughly yet.

As said, in this work we focus on the cubic phase state and we provide explicit protocols to convert a non-Gaussian state that has been recently generated within microwave circuits — namely the trisqueezed state [51] — into a cubic phase state, with simple Gaussian operations that are readily available in the laboratory, in both the optical and the microwave regimes.

More specifically, we introduce two conversion protocols. The first one is a deterministic Gaussian protocol, based on symplectic transformations and displacements. The second one is probabilistic, but — in contrast to the previous protocol — does not require squeezing of the input state. Instead, it uses an ancillary squeezed state and a beam-splitter, a phase

\* zhyu@chalmers.se

rotation, and homodyne measurement. For both protocols, we rely on numerical optimization in order to determine the best parameters to be used, associated with the optical elements listed above.

Before introducing our conversion protocols, we provide a bound on the fidelity to the target cubic phase state that can be achieved with the most-general deterministic Gaussian map. Our deterministic protocol belongs to this class of maps, and in fact we show that it saturates this bound. We then show that our probabilistic conversion protocol allows us to increase the obtainable fidelity with respect to this bound, yet retaining success probabilities that are high compared to existing protocols [39]. This corroborates the trisqueezed state as a resource state that is useful for CV quantum computation.

The paper is structured as follows. In Sec.II we define the input and target states for our conversion protocols, and we motivate their study. In Sec.III A we calculate the upper bound on the fidelity of the state conversion — *i.e.*, the fidelity to the desired target state — obtainable with deterministic Gaussian maps. In Sec.III B we define our deterministic Gaussian conversion protocol, and we show that it corresponds to a simple squeezing and displacement operation on the input mode, achieving high fidelity of conversion — for example, a fidelity of 0.971 for a target cubic non-linearity of approximately 0.156. In Sec.IV, we introduce our probabilistic Gaussian conversion protocol, analyse thoroughly its properties, and show that it yields higher fidelities as compared to the deterministic protocol (for example, up to 0.997 for the same target), for success probabilities as high as 0.051. In Sec.V A we discuss the experimental implementability of our protocols in both microwave and optical systems, before presenting conclusive remarks in Sec.VI. In Appendix A we provide an extensive discussion of the numerical methods used for our optimizations.

## II. PURPOSE OF OUR CONVERSION PROTOCOLS

Before starting, it is useful to recall some standard definitions and notations for CV systems that we are going to use extensively in this paper, as well as the definition of the input and target states. We are going to indicate the vector of quadrature operators for  $N$  bosonic modes as  $\hat{r} = (\hat{q}_1, \hat{p}_1 \dots \hat{q}_N, \hat{p}_N)^T$ , and for each mode we use the following convention for the relation between the quadrature operators and the creation and annihilation operators:  $\hat{q} = (\hat{a} + \hat{a}^\dagger)/2$  and  $\hat{p} = (\hat{a} - \hat{a}^\dagger)/(2i)$ , corresponding to setting  $\hbar = 1/2$ . The squeezing  $\hat{S}(\xi)$ , displacement  $\hat{D}(\beta)$  and phase rotation  $\hat{U}_p(\gamma)$  operators are defined respectively as

$$\hat{S}(\xi) = e^{\frac{\xi^*}{2}\hat{a}^2 - \frac{\xi}{2}\hat{a}^{\dagger 2}}, \quad (1)$$

$$\hat{D}(\beta) = e^{\beta\hat{a}^\dagger - \beta^*\hat{a}}, \quad (2)$$

$$\hat{U}_p(\gamma) = e^{-i\gamma\hat{n}}, \quad (3)$$

with  $\hat{n} = \hat{a}^\dagger\hat{a}$  the number operator,  $\gamma \in \mathbb{R}$ ,  $\beta \in \mathbb{C}$ ,  $\xi \in \mathbb{C}$ , and  $\xi = |\xi| e^{i\phi}$  with  $\phi \in [0, 2\pi]$ .

The successive application of a squeezing and displacement operator onto the vacuum state yields a displaced squeezed state [53]. Its wave function is given by

$$\begin{aligned} \Psi_{\xi, \beta}(q) &= \langle q | \Psi_{\xi, \beta} \rangle \\ &= \langle q | e^{\beta\hat{a}^\dagger - \beta^*\hat{a}} e^{\frac{\xi^*}{2}\hat{a}^2 - \frac{\xi}{2}\hat{a}^{\dagger 2}} | 0 \rangle \\ &= \left( \frac{2}{\pi} \right)^{\frac{1}{4}} \frac{(1 - |\zeta(\xi)|^2)^{\frac{1}{4}}}{\sqrt{1 - \zeta(\xi)}} e^{-\frac{1+\zeta(\xi)}{1-\zeta(\xi)}(q-q_\beta)^2 + 2ip_\beta(q-\frac{q_\beta}{2})}, \end{aligned} \quad (4)$$

where  $|q\rangle$  is an eigenstate of the quadrature operator  $\hat{q}$  with real eigenvalue  $q$ ,  $\zeta(\xi) = \xi \tanh |\xi|/|\xi|$ , and we have introduced the notation  $\beta = q_\beta + ip_\beta$ . Note that in the case of real squeezing parameter, the wave function of a displaced squeezed state reduces to [54]

$$\begin{aligned} \Psi_{|\xi|, \beta}(q) &= \left( \frac{2}{\pi} \right)^{\frac{1}{4}} e^{|\xi|/2} \\ &\exp \left\{ (-e^{2|\xi|}(q - q_\beta)^2 + i2p_\beta q - ip_\beta q_\beta) \right\}. \end{aligned} \quad (5)$$

In the following, we are going to address conversion protocols from an experimental available state to a state that, as said, is known to be pivotal for quantum computation. The input state discussed in this paper is the trisqueezed state defined as [55, 56]:

$$|\Psi_{\text{in}}\rangle = e^{i(t^* \hat{a}^3 + t \hat{a}^{\dagger 3})} |0\rangle. \quad (6)$$

In what follows, we are going to refer to the parameter  $t$  that characterizes the strength of the tri-photon interaction in Eq.(6) as the *triplicity*. Fig.1a shows the Wigner function of the trisqueezed state with triplicity  $t = 0.1 \exp(i\pi/2)$  as an example. As it can be seen, this state is symmetric with respect to the position axis, and it also possess a  $2\pi/3$ -rotational symmetry. The rotational symmetry is a direct consequence of the Hamiltonian generating the state in Eq.(6), and is also reflected in the Fock expansion of the trisqueezed state, where only Fock states with photon numbers that are multiple of three are present [57].

Our target state, the cubic phase state, is defined as [33]

$$|\Psi_{\text{target}}\rangle = e^{ir\hat{q}^3} \hat{S}(\xi_{\text{target}}) |0\rangle. \quad (7)$$

Its wave function is easily computed as

$$\Psi_{\text{target}}(q) = \langle q | \Psi_{\text{target}} \rangle = \left( \frac{2}{\pi} \right)^{\frac{1}{4}} e^{\xi_{\text{target}}/2} e^{-e^{2\xi_{\text{target}}} q_0^2} e^{irq^3}, \quad (8)$$

where the subscript “target” is used in order to distinguish this squeezing parameter from those of other squeezed states that will be introduced later. In what follows, we are going to refer to the parameter that characterizes the strength  $r$  of the cubic interaction in Eq.(7) as the *cubicity*. Fig.1b shows the Wigner function of the cubic phase state with cubicity  $r = 0.0551$  [58]. The state is symmetric with respect to the momentum axis. For convenience, we will fix the squeezing strength of the target state Eq. (8) as 5dB, which implies that  $\xi_{\text{target}} = -\log_{10} \frac{5\text{dB}}{20}$ .

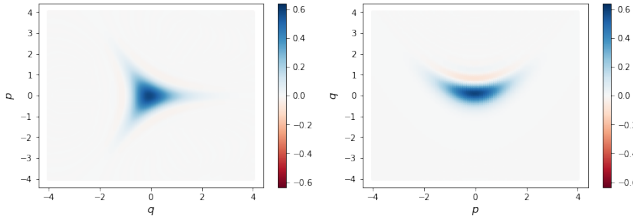


FIG. 1: Wigner functions of the input state (trisqueezed state) and of the target state (cubic phase state) of our protocols. The parameter defining the strength of the triple-photon interaction, i.e. the triplicity, is set to  $t = 0.1 \exp(i\pi/2)$  (corresponding to  $|t| = 0.1$ ), while the corresponding parameter characterizing the cubic phase state, the cubicity, is set to  $r = 0.1558$ , with 5dB squeezing.

In order to fix, for a given input state triplicity, the target state cubicity, we use considerations from quantum resource theory. As said, it has been proved that operations or initial states characterised by negative Wigner functions are necessary for quantum speed up [59]. Wigner negativity is thereby regarded as a resource for computational advantage. A convenient measure of the negativity content of the Wigner function is the Wigner logarithmic negativity or *mana*  $M(\rho) = \log(\int d\vec{r})|W_\rho(\vec{r})|$ , where  $W_\rho(\vec{r})$  is the Wigner function of the state  $\rho$  and where the integral runs over the whole phase-space. The main features of the mana is that it is invariant under Gaussian unitary operations (namely, unitary operations that are generated by Hamiltonian at most quadratic in the canonical bosonic operators), and more generally under deterministic Gaussian protocols [29]. In addition, it does not increase on average under probabilistic Gaussian protocols [29]; namely, one has that

$$M(\rho_{\text{in}}) \geq pM(\rho_{\text{target}}), \quad (9)$$

where  $M(\rho_{\text{in}})$  and  $M(\rho_{\text{target}})$  are the mana of the input and target states, respectively, and  $p$  is the probability of success of the conversion protocol.

Therefore, given that we want to assess both deterministic and probabilistic Gaussian conversion protocols for a given pair of input and target states, it is reasonable to choose the latter states in such a way that they possess the same amount of mana. Given a certain input triplicity, a corresponding cubicity can be estimated numerically by the requirement of keeping the mana invariant. Limited only by numerical accuracy, we choose to start from trisqueezed states with triplicities 0.1, 0.125 and 0.15, while targeting corresponding cubic phase states with the same mana. As a side remark, note that the triple squeezed state Eq.(6) has higher mana than the cubic phase state Eq.(7) for the same average photon number.

Notice that the choice of the target cubicity is not crucial in terms of computational universality, and it is taken here only to ease the quantitative comparison of different protocols. In fact, a cubic phase state of any given cubicity  $r$  can be used to generate a unitary operation of the form  $\exp[i\hat{r}\hat{q}^3]$ ,

via Gaussian deterministic gate teleportation [33]. The latter is usually denoted as cubic phase gate and, equipped with arbitrary Gaussian unitaries, unlocks universality for any value of  $r$  [26]. In fact, it is easy to show that  $\hat{S}(s)^\dagger \exp[i\hat{r}\hat{q}^3] \hat{S}(s) = \exp[i\hat{r}e^{3s}\hat{q}^3]$ , where  $s$  is the strength of a squeezing gate. In other words, under the assumption of having at disposal arbitrary squeezing, the non-linearity can be enhanced or reduced by changing the strength of a supplementary squeezing gate.

In order to characterise conversion protocols that map the trisqueezed state onto the cubic phase state or aim at approximating the latter as well as possible, we need to define a measure of the distance between the target state and the transformed input state. For this we choose the fidelity

$$\mathcal{F}(\rho_1, \rho_2) = \left( \text{Tr} \left\{ \sqrt{\sqrt{\rho_1}\rho_2\sqrt{\rho_1}} \right\} \right)^2. \quad (10)$$

As our target state is a pure state, this expression can be simplified to

$$\mathcal{F}(\rho, \Psi_{\text{target}}) = \langle \Psi_{\text{target}} | \rho | \Psi_{\text{target}} \rangle. \quad (11)$$

In what follows, we detail two Gaussian protocols enabling the approximate conversion of a trisqueezed state onto a cubic phase state, and we characterise their performances.

### III. DETERMINISTIC GAUSSIAN CONVERSION PROTOCOL

In this section we introduce our deterministic Gaussian conversion protocol. Before doing so, we provide numerically an upper-bound to the fidelity of conversion that can be achieved by the class of trace-preserving Gaussian completely-positive (CP) maps, and we show that our deterministic protocol saturates this bound. In other words, the optimal maps are symplectic maps with displacement, and we show that the dominant contribution consists of squeezing. In this section, we will consider for simplicity an input trisqueezed state with real and positive triplicity [see Fig.2 (a)], which makes the effect of squeezing towards state conversion apparent.

#### A. Fidelity bound with general Gaussian maps

Trace-preserving Gaussian completely-positive maps can be understood as all the completely-positive maps that map Gaussian states into a Gaussian state. These maps are characterized by their action onto the symmetrically ordered characteristic function [25]:

$$\chi_\rho(\vec{r}) = \text{Tr} \left\{ \hat{D}(-\vec{r}) \rho \right\} = \sum_{n,n'=0}^{\infty} \rho_{nn'} \langle n' | \hat{D}(-\vec{r}) | n \rangle \quad (12)$$

with the arbitrary displacement operator being

$$\hat{D}(-\vec{r}) = e^{-i(\vec{r}^T \Omega \hat{r})}, \quad (13)$$

with  $\vec{r} \in \mathbb{R}^{2N}$  and

$$\Omega = \bigoplus_{j=1}^N \begin{pmatrix} 0 & 1 \\ -1 & 0 \end{pmatrix}$$

being the symplectic form for  $N$  modes. For speeding-up the numerical calculation of the characteristic function, it will be useful to use the matrix elements of the displacement operator appearing at the RHS of Eq.(12). They can be written for  $m \geq n$  as [60]

$$\langle m | \hat{D}(\alpha) | n \rangle = \sqrt{\frac{n!}{m!}} e^{-|\alpha|^2/2} \alpha^{m-n} L_n^{m-n}(|\alpha|^2) \quad (14)$$

and for  $m \leq n$

$$\langle m | \hat{D}(\alpha) | n \rangle = \sqrt{\frac{m!}{n!}} e^{-|\alpha|^2/2} (-\alpha^*)^{m-n} L_m^{n-m}(|\alpha|^2), \quad (15)$$

where  $L_m^{n-m}(|\alpha|^2)$  are the associated Laguerre polynomials.

The action of a trace-preserving Gaussian CP-map  $\Phi$  on the characteristic function is then given by [61]:

$$\chi_\rho(\vec{r}) \rightarrow \chi_{\Phi(\rho)}(\vec{r}) = e^{-\frac{1}{4}\vec{r}^T \Omega^T Y \Omega \vec{r} + i\vec{l}^T \Omega \vec{r}} \chi_\rho(\Omega^T X^T \Omega \vec{r}) \quad (16)$$

with  $X, Y$  being  $2N \times 2N$  real matrices,  $\vec{l}$  being a  $2N$  real vector,  $Y$  being symmetric, and fulfilling the following positive semi-definite matrix constraint:

$$Y \pm i(\Omega - X \Omega X^T) \geq 0. \quad (17)$$

Notice that Eq. (17) in turn implies that  $Y$  has to be a positive semi-definite matrix. The requirement for positive semi-definiteness needs to hold for both signs, since transposition does not affect the positive (semi-) definiteness of a matrix.

Since the conversion protocol we are investigating is one mode to one mode only, we set  $N = 1$  in the following paragraphs. In order to determine numerically the matrices  $X, Y$  and the vector  $\vec{l}$  that map the trisqueezed state to the cubic phase state (for a given pair of cubicity and triplicity parameters), or approximate it as good as possible, we re-express the fidelity defined in Eq. (11) in terms of the characteristic functions of the input and target states:

$$\mathcal{F}(\rho, \rho_{\text{target}}) = \text{Tr}\{\rho \rho_{\text{target}}\} = \frac{1}{4\pi} \int d\vec{r} \chi_\rho(\vec{r}) \chi_{\rho_{\text{target}}}(-\vec{r}), \quad (18)$$

where  $\rho_{\text{target}} = |\Psi_{\text{target}}\rangle \langle \Psi_{\text{target}}|$ . We calculated numerically the characteristic functions for both the input and target state given respectively by Eqs. (6) and (7) and then transformed the input characteristic function given the trace-preserving Gaussian CP-map in Eq. (16). We then maximised the fidelity between the transformed state and the target state by optimizing  $X, Y$  and  $\vec{l}$ , while still fulfilling Eq. (17). As mentioned, since this optimization involves a number of potential

evaluations of the characteristic functions, using the analytical expressions for the matrix elements of the displacement operator in Eqs.(14) and (15) significantly speeds-up the computation, compared to direct matrix exponentiation. More details regarding the numerical calculations are provided in Appendix A.

The results of this fidelity optimization are shown in Table I, for various values of the triplicity of the input trisqueezed state. For the value of triplicity  $t = 0.1$ , we obtain a conversion fidelity of 0.9708. The fidelity of conversion decreases at increasing triplicity. The parameters in terms of the matrices  $X, Y$  and  $\vec{l}$  that optimize the conversion are given in the Appendix, in Table VI.

By looking at the optimized parameters, a few considerations can be made. The matrix  $Y$  is essentially trivial, implying that the conversion can be done unitarily. Furthermore,  $X$  is diagonal with perfect reciprocal entries, i.e. it corresponds to squeezing. The vector  $\vec{l} = \begin{pmatrix} l_q \\ l_p \end{pmatrix}$  has a non-trivial contribution for the displacement  $l_p$ , the displacement along the  $p$  axis, so we expect that a purely symplectic conversion will not saturate the bound given by the trace-preserving Gaussian completely-positive maps. This result can be understood at an intuitive level:  $Y$  should be close to zero, so we do not add any noise to the conversion; the displacement in  $p$  should be zero to conserve the symmetry between both Wigner functions, and positive in  $q$ , to match the maxima of their respective Wigner functions. Finally, as we will show in the next paragraph, an exact conversion can be done asymptotically with only squeezing.

## B. Symplectic Conversion Protocol

We now specialize to the case of symplectic transformations, which allows us to design a specific deterministic conversion protocol. Symplectic transformations are special cases of the protocols introduced in Sec.III A and correspond to unitary operations only, i.e. the noise matrix  $Y$  is zero and  $X \in Sp_{2,\mathbb{R}}$  is a symplectic matrix [1].

We denote the unitary operation associated to  $X$  as  $\hat{U}_X$ , acting as follows on the trisqueezed state:

$$\hat{U}_X e^{it(\hat{a}^3 + \hat{a}^{\dagger 3})} |0\rangle = \hat{U}_X e^{it(\hat{a}^3 + \hat{a}^{\dagger 3})} \hat{U}_X^\dagger \hat{U}_X |0\rangle. \quad (19)$$

For exact state conversion, the following relation needs to hold:

$$\hat{U}_X e^{it(\hat{a}^3 + \hat{a}^{\dagger 3})} \hat{U}_X^\dagger \rightarrow e^{ir\hat{q}^3}. \quad (20)$$

This can be achieved asymptotically in the infinite squeezing limit. Squeezing implements a Bogoliubov transformation

$$\hat{a} \rightarrow \hat{S}(\xi) \hat{a} \hat{S}^\dagger(\xi) = u\hat{a} + v\hat{a}^\dagger \quad (21)$$

$$\hat{a}^\dagger \rightarrow \hat{S}(\xi) \hat{a}^\dagger \hat{S}^\dagger(\xi) = u^* \hat{a}^\dagger + v^* \hat{a} \quad (22)$$

with  $u = \cosh(|\xi|)$  and  $v = \sinh(|\xi|) e^{-i\phi}$  (see Eq. (1)) In the case of  $u = v$  and  $u^* = v^*$ , this transformation gives

us the required form, because  $\hat{q} \propto \hat{a} + \hat{a}^\dagger$ . This means that a conversion with asymptotically unit fidelity is possible for  $|\xi| \rightarrow \infty$  and  $\phi = 0$ . Since the squeezing parameter  $\xi_{\text{target}}$  associated with the target cubic phase state Eq.(7) is finite, one expects that the obtained squeezing operation will be a trade-off between matching the target state squeezing and transforming the trisqueezed state.

Similarly to Sec. III A, we determine the maximum fidelity between the input and target states that is achievable with symplectic transformations by transforming the input characteristic function. The advantage with respect to the general Gaussian maps of section III A is that here, since we know that  $X \in Sp_{2,\mathbb{R}}$ , we can parametrize the transformation as [62]:

$$X = \begin{pmatrix} g & ge \\ cg & g^{-1} + cge \end{pmatrix}, \quad (23)$$

for  $g, e, c \in \mathbb{R}$  and  $g$  non-zero. In other words, we are using 3 real parameters to parametrize a real symplectic transformation, which is precisely the dimension of the real symplectic group  $Sp_{2,\mathbb{R}}$ .

Fig. 2b shows the Wigner function of the output state corresponding to the optimization of the symplectic transformation in Eq. (23). It can be seen that the Wigner function of the output state and that of the target state in Fig.1b are qualitatively similar, which is expected as the fidelity is equivalent to the Wigner overlap [63]. The results of the optimizations are shown in Table I. Squeezing is the dominant contribution of the symplectic transformation, with the off-diagonal elements in the symplectic matrix being negligible small, as can be seen in Appendix B.

Interestingly, from Table I we see that the obtained values for the fidelity of conversion are, for all values of triplicity, below the ones from the Gaussian maps. This is to be expected, since the optimal Gaussian maps had a non-vanishing contribution of displacement. The effectiveness of squeezing on the input state towards reaching a cubic phase state can also be intuitively understood from Fig.2.

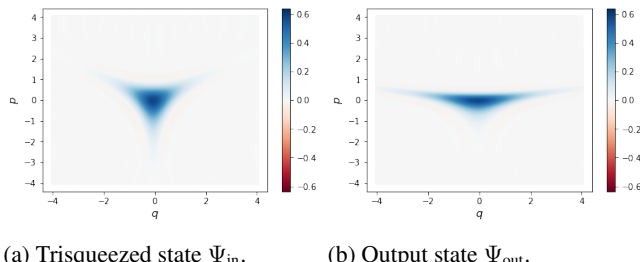


FIG. 2: Wigner function of the output state obtained via our deterministic Gaussian conversion protocol  $\Psi_{\text{out}}$ , excluding the final displacement. The triplicity of the input state is 0.1.

As we have seen, given only symplectic single-mode transformations, squeezing is the relevant contribution. An intuitive extension to the investigated purely symplectic transformations and motivated by the results obtained from the trace-preserving Gaussian completely-positive maps are displace-

ments. The characteristic function transforms under displacements as:

$$\chi_\rho(\vec{r}) \rightarrow \chi_{\hat{D}(\vec{l})\rho\hat{D}(\vec{l})^\dagger}(\vec{r}) = e^{i\vec{l}^T \Omega \vec{r}} \chi(\vec{r}). \quad (24)$$

In the high squeezing limit negligible contributions of displacements are expected, since they add lower orders of operators in the exponent of the input state in Eq. (6). However the target state contains finite squeezing  $\xi_{\text{target}}$  instead of being infinitely squeezed and thus these contribution cannot be neglected. Since the off-diagonal terms in the symplectic case were trivial, we focus on squeezing and displacement only. The resulting conversion scheme is depicted in Fig.3.

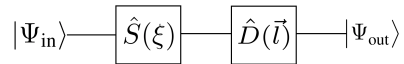


FIG. 3: Sketch of our deterministic Gaussian conversion protocol. We apply a squeezing operator and a displacement on a trisqueezed state.  $|\Psi_{\text{out}}\rangle$  is the output state after optimizing the parameters in the circuit.

The optimized fidelities for this approach are shown in Table II as well as the parameters for the optimized protocol. The maximum achieved fidelity is improved further with displacements in  $q$ , achieving the value of 0.971 and saturates the bounds given by the Trace-preserving Gaussian completely-positive maps.

Note that in the present case of symplectic transformations, the achieved output state has the same mana as the input state, because unitary Gaussian operations conserve the Wigner negativity [29].

#### IV. PROBABILISTIC GAUSSIAN CONVERSION PROTOCOL

In Ref.[39], a tunable optical circuit for the probabilistic generation of a cubic phase starting from ancillary squeezed states and using photon counting was introduced, where the parameters were optimized to achieve the best fidelity.

Inspired by these results, we introduce our probabilistic protocol for the conversion of the trisqueezed state into a cubic phase state. This conversion protocol is sketched in Fig. 4. It takes as inputs a trisqueezed state, Eq.(6), in the upper rail and a displaced squeezed state, Eq.(4), in the lower rail. These are fed into a beam-splitter corresponding to the symplectic transformation  $U_{\text{BS}}^{\text{R}}(2\theta)$ , where

$$U_{\text{BS}}^{\text{R}}(2\theta) = \begin{pmatrix} \cos \theta & \sin \theta \\ -\sin \theta & \cos \theta \end{pmatrix}. \quad (25)$$

Notice that the 2x2 matrix in Eq.(25) refers to two modes, i.e. is meant to act on the annihilation operators  $\hat{a}_1, \hat{a}_2$ , in contrast to the 2x2 matrices of the previous sections and in particular of Eq.(23), acting on the annihilation and creation operators of a single bosonic mode. Next, a phase rotation, Eq.(3), is performed on the lower rail and a homodyne measurement

Triplicity	Cubicity(5dB)	Gaussian CP-map	Symplectic
0.1	0.1558	0.9708	0.9335
0.125	0.2757	0.9273	0.8810
0.15	0.4946	0.8557	0.8113

TABLE I: Maximized fidelities for Gaussian CP-maps (third column), purely symplectic maps (fourth column), for different input-target pairs (first and second column). The optimized parameters are in Appendix B.

Triplicity	Cubicity(5dB)	Fidelity	Squeezing	Displacement $l_p$	Displacement $l_q$	Mana <sub>out</sub>
0.1	0.1558	0.9708	0.6741	0.1547	$2 \cdot 10^{-9}$	0.1658
0.125	0.2757	0.9273	0.7816	0.2268	$-10^{-8}$	0.3338
0.15	0.4946	0.8557	0.9463	0.3029	$-5 \cdot 10^{-8}$	0.5450

TABLE II: Maximized fidelities and optimized parameters for the Gaussian protocol including squeezing and displacement, as depicted in Fig. 3, for different input-targets pairs. The last column is the mana of the transformed state.

is performed on the upper rail. Upon post-selection on the measurement result  $q = 0$  on the upper rail, a displacement is performed on the state on the lower rail.

Notice that the deterministic protocol analyzed in Sec. III B, which makes use of active in-line squeezing, could be converted to a (deterministic) protocol that uses only off-line squeezing. Ideally, this could be accomplished via a gate-teleportation gadget [26, 64–66] composed of a control-phase gate whose two input modes are fed by the trisqueezed input state and an auxiliary infinitely squeezed state; an additional phase-space rotation and a final displacement of the latter mode, conditioned on the outcome of an ideal homodyne measurement on the first mode, would implement the required transformation. Here we follow a similar strategy, where however we use the more realistic assumptions of finite squeezing, finitely resolved homodyne detector, non-conditional displacement, and we use a standard beam-splitter operation between the modes. This in turn implies that the protocol here proposed is probabilistic but closer to experimental implementations (see also Sec. V).

As an additional remark, it is interesting to compare our conversion protocol to the synthesis protocols in Refs. [39] and [40]. In these, the non-Gaussian element was provided, respectively, by the measurement (photon-number resolving detector) and by nonlinear media (self Kerr effect). This in contrast to our scheme in which the non-Gaussian element is inherent to the input state.

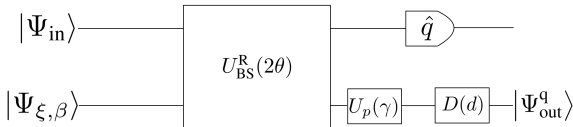


FIG. 4: Sketch of our probabilistic Gaussian conversion protocol. We apply a beam-splitter  $U_{BS}^R(2\theta)$  on a trisqueezed state and an ancillary squeezed state. After a rotation  $U_p(\gamma)$ , we post-select the homodyne measurement on the first mode to value  $q = 0$  and displace the second mode with  $D(d)$ .  $\Psi_{out}^q$  is the output state after optimizing the parameters in the circuit.

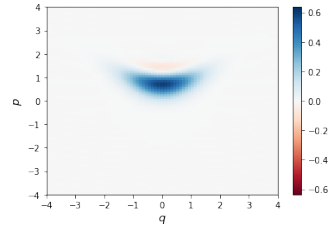


FIG. 5: Wigner function of the output state  $|\Psi_{out}^q\rangle$  of the probabilistic Gaussian conversion protocol, starting from the trisqueezed state with triplicity of 0.1. The corresponding parameters of the circuit are shown in the first row of Table III.

We now calculate explicitly the output state of the circuit sketched in Fig. 4. To simplify the calculation, we consider the output state before the displacement on the lower mode. This is equivalent to displace the target state by the opposite displacement in terms of overlap between the two states. In other words, the fidelity is the same whether we displace the output state, or the target state by the opposite displacement.

Note that the quadrature operator  $\hat{q}$ , associated with ideal homodyne detection, has eigenvalues  $q$  in the real axis. Then, the probability to measure a particular one of these is infinitely small. In order to overcome this limitation, and properly model a finite-resolution homodyne detector, the real axis can be discretized into bins of width  $2\eta$  around the real values  $q_n$ , where  $n \in \mathbb{Z}$  is the integer labelling the  $n$ -th bin. To each measurement result  $q_n$  is therefore associated the probability that the measurement results fall within the  $n$ -th bin. In particular, the probability of obtaining  $q_n = 0$  defines the success probability of our protocol. As a result, the output state of our protocol, given by the conditional density matrix, is a mixed state.

As shown in Appendix C, the output state that corresponds to a general measurement outcome  $q$  associated to an infinitely

resolved homodyne detector can be written as:

$$\begin{aligned} & |\Psi_{\text{out}}^q(\xi, \beta, \theta, \gamma)\rangle \\ &= \frac{1}{\pi} \int dq_2 d\alpha \Psi_{\text{in}}(q \cos \theta + q_2 \sin \theta) \\ & \quad \Psi_{\xi, \beta}(-q \sin \theta + q_2 \cos \theta) \langle \alpha | q_2 \rangle | \alpha e^{-i\gamma} \rangle, \end{aligned} \quad (26)$$

where the displaced squeezed state parameters  $\xi$  and  $\beta \equiv q_\beta + ip_\beta$  are complex numbers, while the angle  $\theta$  parameterizing the beam-splitter and the phase rotation  $\gamma$  are real numbers. As a result, the output state obtained by considering a finite-size bin is given by the conditional density matrix

$$\hat{\rho}_{n, \text{cond}} = \frac{1}{\text{Prob}[q_n]} \int_{q_n - \eta}^{q_n + \eta} dq |\Psi_{\text{out}}^q\rangle \langle \Psi_{\text{out}}^q|, \quad (27)$$

where  $|\Psi_{\text{out}}^q\rangle$  is given in Eq.(26), and where  $\text{Prob}[q_n]$  is the probability of obtaining outcome  $q_n$ , given by

$$\begin{aligned} \text{Prob}[q_n] &= \int_{q_n - \eta}^{q_n + \eta} dq \int dq_2 \\ & \Psi_{\text{in}}^*(q \cos \theta + q_2 \sin \theta) \psi_{\text{in}}(q \cos \theta + q_2 \sin \theta) \\ & \Psi_{\xi, \beta}^*(q_2 \cos \theta - q \sin \theta) \psi_{\xi, \beta}^*(q_2 \cos \theta - q \sin \theta). \end{aligned} \quad (28)$$

The fidelity defined in Eq.(10) between the target state and the output conditional density matrix in Eq.(27) is then expressed as

$$\begin{aligned} F_{q_n} &= \langle \Psi_{\text{target}} | \hat{\rho}_{n, \text{cond}} | \Psi_{\text{target}} \rangle \\ &= \frac{1}{\text{Prob}[q_n]} \int_{q_n - \eta}^{q_n + \eta} dq |\langle \Psi_{\text{target}} | \Psi_{\text{out}}^q \rangle|^2. \end{aligned} \quad (29)$$

We focus in particular in  $q_n = 0$ .

There are seven parameters that can be optimized for maximizing the fidelity in Eq.(29), including the displacement parameter  $d$  after the measurement. The numerical optimization of the fidelity is hence a challenging task. It involves three computationally expensive numerical integrations, and the total necessary time grows exponentially with the dimension of the space to be explored. However, we empirically find that, as a consequence of the symmetries of the input and target states, some of the parameters can be fixed. As shown in Fig. 1a, the Wigner function of the trisqueezed state is symmetric with respect to the position axis, while the target state is symmetric with respect to the momentum axis (Fig. 1b). We fix the phase of the ancillary displaced squeezed state so as to yield a position-squeezed state, i.e.,  $\xi$  real and positive, and we consider a real displacement for the ancillary squeezed state, hence  $p_\beta = 0$ . With these choices, the full two-mode input state is symmetric with respect to the position axis. Then, we set the phase rotation to  $\gamma = \pi/2$  so that our output state upon post-selection over  $q_n = 0$  has the same symmetry of the target state, i.e., it is symmetric with respect to the momentum axis. Hence, we are left with tuning the magnitudes of the squeezing and displacement parameters, the real beam-splitter parameter and the final momentum displacement, in order to achieve the maximal fidelity to our target state. In Appendix D

we provide an analysis of how the various tunable parameters in our protocol affect the properties of the output states.

We carry the numerical optimizations by running three independent codes, namely one Python code running on a personal computer, one C++ code running in serial on central processing units (CPUs) in a cluster environment, and finally a CUDA [67] code running in parallel on graphics processing units (GPUs) [68] in a cluster environment. We provide the relevant details on these approaches in Appendix A.

### A. Conversion protocol performance at fixed input mana

In order to compare our results with those obtained in Sec.III, we first consider the case where the target state has the same mana as the input trisqueezed state, which is always also the case for the deterministic maps. The mana in the target state is determined by the parameters  $r$  and  $\xi_{\text{target}}$ . However, we will only come as close as possible to this state with our probabilistic protocol. Therefore, we expect that the output mana will not be the same as the one of the input state. We anticipate that the deviations may be significant because the mana is an extremely sensitive quantity, that can very significantly even if the overlap (quantified by the fidelity) of two states is very high.

As can be seen in Fig. 5, the Wigner function of the output state is qualitatively similar to the one of the target state (Fig. 1b). Table III shows the results for the achieved fidelity of conversion after optimizing the tunable parameters in our probabilistic protocol. We can see that a fidelity as high as 0.997 can be obtained with success probability of 5% when the triplicity of the input state is moderate. As can be observed in Table III, and as expected, the mana obtained in the output state of our protocol can be sensibly different as the one of the target state, despite high fidelity.

Let us stress that it is quite remarkable that the trisqueezed state can be transformed to the cubic phase state via a probabilistic protocol with such high fidelity. In view of the considerations above it is however possible to provide an intuitive explanation for this. In fact, we have seen in Sec.III that a squeezing operation is successful in the conversion and, as said, the probabilistic protocol that we have presented in this section can be interpreted as a squeezing operation via gate teleportation (see also Appendix E).

### B. Conversion protocol performance at varying input mana

We now relapse the requirement that the target state must possess the same mana as the input state. Eq. (9) implies that the mana will still be conserved on average, even when we are targeting a state with higher mana with respect to the one at the input, which will succeed with a certain probability. So, what is the performance of our protocol when we start from an input state with lower, or higher, mana with respect to the one of the target state? Fig. 6 shows fidelity and success probability of our protocol, as a function of the mana in the input

Triplexity	Mana <sub>in</sub>	Fidelity	Probability	$\theta$	$q_\beta$	$\xi$	d	Mana <sub>out</sub>
0.1	0.1576	0.9971	0.0513	0.8987	-0.9121	0.3011	-1.1751	0.1103
0.125	0.3350	0.9866	0.0434	0.7992	-1.2153	0.001	-1.1104	0.1945
0.15	0.5737	0.9284	0.0508	0.6378	-0.001	1.4184	-1.3639	0.2197

TABLE III: Fidelity, Success probability, and optimal circuit parameters when targeting a state with the same mana with the input mana.  $\theta$  is the parameter in beam-splitter.  $\xi$  is the squeezing strength.  $q_\beta$  is the displacement of position of the squeezed state. d is displacement of the output state in p direction.

state, for fixed target state mana. The dashed line in Fig. 6 corresponds to the (fixed) mana in the target state. On the left of this line, i.e., when the mana of the input is smaller than that of the target state, the obtained high fidelity represents hence a probabilistic concentration protocol. We observe that this is possible to achieve with success probabilities of 0.05. On the right of the dashed line we observe that the fidelity does not increase when having higher mana in the input state. However, there is a positive correlation between the success probability and the input mana. Moreover, the fidelity is robust against a certain decrease of the input mana, while dropping quickly when the input mana is below 0.01. At each point of the figure, the bound of Ref. [29] is satisfied, as can be verified by multiplying the mana of the output state with the success probability.

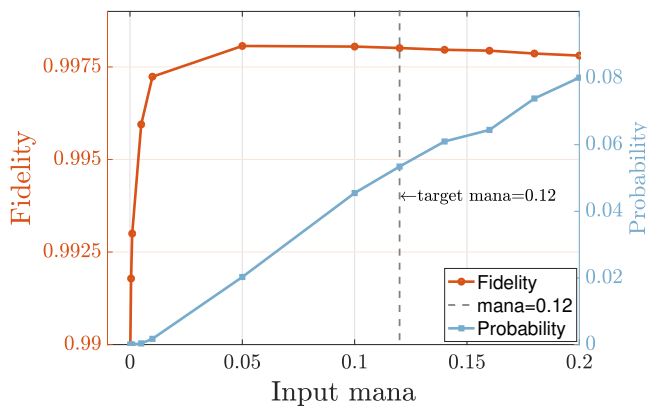


FIG. 6: Fidelity and success probability of the probabilistic conversion protocol as a function of the mana of the input state. The mana of the target state here is fixed at 0.12, corresponding to a cubicity of  $r = 0.133$ . In turn, this value of cubicity corresponds to the value for which we obtain the fidelity value 0.997, see Table III.

Finally, in Fig. 7, we analyse the effect of the width  $\eta$  of the acceptance region on the success probability, as well as on the fidelity of our protocol. As expected, for larger values of  $\eta$ , the fidelity decreases due to the lower purity of the output state Eq.(27), while the success probability Eq.(28) increases.

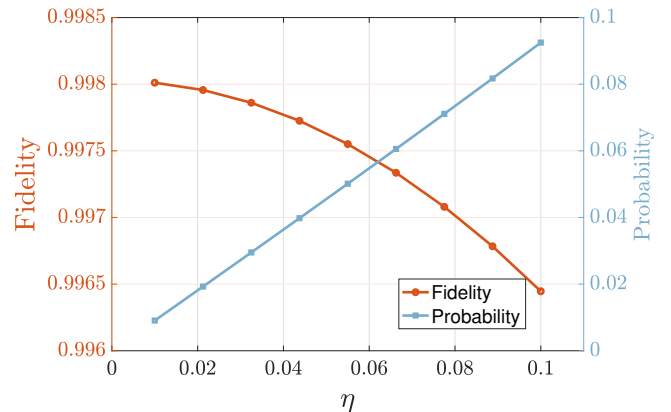


FIG. 7: Fidelity and success probability as a function of the width of the acceptance region  $\eta$ .

## V. EXPERIMENTAL IMPLEMENTABILITY OF THE PROTOCOLS

In this Section, we discuss the feasibility of our protocol in state-of the art experiments, based either on microwave circuits and Josephson junctions, or on optical systems.

### A. Microwave circuits and residual Kerr terms

In superconducting microwave circuits, the field commonly referred to as circuit QED, nonlinear interactions between microwave photons are mediated by Josephson junctions or Josephson junction-based devices such as the Superconducting QUantum Interference Device (SQUID) [69, 70]. Arranging Josephson junctions in loops allows for magnetic flux biasing. This, in turn, gives the possibility to drive different parametric processes when these devices interact with superconducting resonators.

It is well-established that in the linear regime, SQUID-mediated interactions between microwave modes allow for engineering Gaussian operations such as squeezing or beam-splitting required for our proposal [71–73]. The full set of linear operations follows trivially with the addition of monochromatic microwave tones which implement linear displacements. Finally, homodyne detection can be implemented via phase-sensitive parametric amplification [74]. The highest quantum efficiency reported today for homodyne measurement in microwave circuits is about 0.7 [75]. For the purpose

of our deterministic protocol this will imply to first release the resonator field in a controlled fashion. This can be done, for instance, following [76].

Similarly, higher-order processes can be exploited from the SQUID nonlinearity. Recently, the three-photon drive Hamiltonian giving rise to the trisqueezed state studied in this work, Eq.(6), has been realized experimentally [48, 51]. Nevertheless, a residual Kerr interaction is unavoidable in these implementations, which might be detrimental for the protocols presented here.

In order to assess the robustness of our probabilistic conversion protocol outlined in Sec.IV against imperfections in the input state due to the residual Kerr interaction, we repeat the fidelity optimization over the circuit parameters when we introduce a Kerr deformation in the input state, for various strength of the residual Kerr. We perform this analysis for the probabilistic protocol because it is the one yielding the highest conversion fidelity. The results are reported in Table IV. High fidelities and success probability can still be obtained when the Kerr interaction parameter is weak as compared to the triplicity. We conclude that our results are stable in the case where an unwanted Kerr non-linearity introduced by the SQUID affects the generation of the trisqueezed state [51].

$t/\text{Kerr}$	5	2.5	1
fidelity	0.99523	0.99137	0.97966
probability	0.08970	0.1184	0.13373

TABLE IV: Fidelity and success probability of our probabilistic conversion protocol when a Kerr deformation is introduced in the input state.

In microwave applications, losses due to the external environment are unavoidable. Nevertheless, state-of-the-art 3D cavities can achieve quality factors of the order of  $10^6$  [50]. On the other hand, the squeezing and Kerr interactions can be designed to achieve strengths in the tenths of MHz. These interaction strengths, combined with the ability to apply fast coherent pulses, allows for operating these devices faster than dissipation effects take place.

## B. Optical systems

In quantum optics, availability of ancillary squeezed states characterized by squeezing parameters ranging from a few to 15dB [77, 78], beam splitters and homodyne detection, i.e. the elements composing our probabilistic conversion protocol introduced in Sec.IV, is well established. Hence, our probabilistic conversion protocol can be implemented with technology that is readily available in quantum optics labs. Squeezing in-line, i.e. application of a squeezing operator on a state that is not vacuum, as it is required by our first protocol, is regarded as more challenging. In this sense, the probabilistic protocol presented in this paper appears to be easier to implement than the deterministic protocol when it comes to optical implementations. Also note that implementability of the present protocols in optical devices holds in contrast to the proposal

of Ref. [5], where only microwave architectures are discussed.

We recall that the generation of triple-photon states - a three-mode version of our trisqueezed states, corresponding to the Hamiltonian  $a_1^\dagger a_2^\dagger a_3^\dagger + \text{h.c.}$  - has been already proposed theoretically in Ref. [79]. Third and higher-order processes in spontaneous parametric down conversion and other non-linear parametric interactions have also been analysed theoretically in Ref. [80].

## VI. CONCLUSIONS AND PERSPECTIVE VIEWS

In this paper, we have studied two Gaussian conversion protocols that allow one to convert an experimentally available non-Gaussian state, namely the trisqueezed state, onto a known resource state for universal quantum computation over continuous variables, the cubic phase state.

Depending on the experimental set-up and on the needs, one or the other conversion method might be preferable. Our first protocol presents the advantage of being deterministic, while requiring in-line squeezing — possible in micro-wave set-ups, while challenging in quantum optical ones. On the other hand, our second protocol is probabilistic, but achieves higher fidelities and could be implemented using off-line squeezing — therefore feasible in various platforms, in particular both within optical and microwave set-ups. The squeezing required in the two protocols, relative to the conversion with highest fidelity, is of the order of 6 dB and 2.6 dB respectively, both achievable in either microwave or optical devices.

An interesting question that needs to be addressed in order to conclude unequivocally that the trisqueezed state allows one to promote a Gaussian set of gates to fault-tolerant, universal quantum computation is whether the achieved conversion fidelity is enough in order to generate fault-tolerantly GKP states [22]. This can be assessed by using the obtained cubic phase state for implementing a cubic phase gate by gate teleportation [33], and by subsequently using a probabilistic protocol for GKP states generation from cubic phase gates, and Gaussian resources [34]. In this way, the use of qubit error-correction codes concatenated to the GKP code allows one to determine a target fidelity for the generated GKP states. This target fidelity, in turn, is translated into a requirement for the fidelity of the cubic phase states. We leave this analysis for future work.

Note that the approach that we have developed for the study of our probabilistic protocol, namely the calculation of the output fidelity provided in Appendix C, Eq.(C17), combined with the numerical optimization tools detailed in Appendix A, are valid for arbitrary input, ancillary state and target state. Therefore, our approach can be readily employed, upon replacement of the input and target wave functions, for the study of further arbitrary conversion protocols. The study of these extensions is an interesting perspective stemming from our work. Ultimately, Gaussian conversion protocols can shed light on the resourcefulness of generic non-Gaussian states for universal quantum computation.

## VII. ACKNOWLEDGEMENTS

O. H. and Y. Z. contributed equally to this work. We thank Chris Wilson, Timo Hillmann, Laura Garca-Ivarez and Simone Gasparinetti for fruitful discussions. G.F. acknowledges support from the VR Grant QuACVA. F. Q., Y. Z., G. F. and O. H. acknowledge support from the Wallenberg Center for Quantum Technology (WACQT). The numerical computations were performed on resources at Chalmers Centre for Computational Science and Engineering provided by the Swedish National Infrastructure for Computing.

### Appendix A: Details on the numerical optimization

In both the probabilistic and deterministic protocols, the fidelity is a relatively expensive function to evaluate numerically, making the numeric optimization challenging. To tackle this challenge, we turned to high-performance computing, and tried different numerical optimization strategies. Furthermore, for each protocol, we developed three independent implementations that were benchmarked against each other, and against analytic calculations, to ensure numeric consistency. The first two codes were implemented in Python and C++ to run in serial on central processing units (CPUs), and the third code in CUDA [67, 81] for high-performance computing and massive parallelization on NVIDIA Tesla V100 graphics processing units (GPUs). The Python code was run on personal computers (both laptop and desktop machines), while the C++ and CUDA codes were run both on personal computers and on a computer cluster.

For the probabilistic protocol, the Python code used the library GPyOpt [82] and Bayesian optimization (BO) [83, 84], while the C++ and CUDA codes used the library Thrust [85–87] and particle swarm optimization (PSO) [88, 89]. For the deterministic protocol, the Python code used the library QuTiP [90, 91] with BFGS optimization [92–95], while the C++ and CUDA codes used the libraries Thrust, Armadillo [96, 97] and OptimLib [98] with both particle-swarm optimization and differential evolution optimization (DE) [99]. Both particle-swarm optimization and differential evolution are inspired by natural evolution, and were chosen because they are versatile methods with good performance in higher dimensions, and are easy to parallelize efficiently. In contrast to many quasi-Newton methods, they do not rely on the gradient of the objective function (the function to be minimized, i.e. one minus the fidelity), and can get out of local minima. Similarly, Bayesian optimization does not rely on the gradient, and was chosen as it is a powerful and popular method for global optimization. BFGS, which is a quasi-Newton method, was chosen for comparison. Some of these methods are described in greater detail further below.

In the end, all implementations gave the same results for the same choice of input parameters, and all the optimization methods eventually found the same maxima in the fidelity. The CUDA implementation managed to properly harness the performance of the GPUs [68], and was therefore more than an order of magnitude faster than the C++ im-

plementation (measured in number of fidelities evaluated per second), which in turn was more than an order of magnitude faster than the Python implementation.

Since the integrands in Eqs. (18) and (29) behave smoothly as a function of the integration parameters, the triple integrals in the deterministic and probabilistic Gaussian conversion protocol can be calculated using standard numeric integration. In both optimization algorithms, we limited the range of the optimization parameters by the following arguments.

Table. V shows the range for  $\theta, q_\beta, \xi$  and  $d$ . The bounds for the displacement are limited by the probability, which decreases exponentially with the displacement of the input state.

$\theta$	$q_\beta$	$\xi$	$d$
$[0, \pi/2]$	$[0, 1.5]$	$[0, 1]$	$[-3, 0]$

TABLE V: The bounds for optimizing parameters

The Bayesian and particle-swarm optimization strategies will now be explained in greater detail.

### 1. Bayesian optimization

Bayesian optimization [83, 84] (BO) is a global optimization algorithm which is applied for the search of optimal parameters in computationally expensive functions. The general BO algorithms iterates between function evaluations and predictions about optimal parameters, and terminates when a certain number of iterations have been executed. Writing the optimization parameters at iteration step  $i$  in a vector  $\mathbf{x}_i$ , BO tries to minimize the number of function evaluations by carefully selecting the next point  $\mathbf{x}_{i+1}$  where to compute the objective function. In each iteration step, BO considers the complete history of so far collected points  $\mathbf{x}_i$  and function evaluations.

The two main component of BO are (i) a prior probabilistic belief of an objective function and (ii) an acquisition functions [100]. The prior probabilistic belief of the objective function is in general sampled from a Gaussian process. The obtained value of the objective function is then used in the acquisition function, which determines the optimization parameters for the next position  $\mathbf{x}_{i+1}$ . In our approach, we applied the square exponential kernel as a model of similarity in a Gaussian process, and the expected improvement criterion as acquisition function. The maximal number of iterations was obtained empirically by running the algorithm several times and benchmarking with the optimal values predicted by PSO. Our implementation uses the library GPyOpt [82] for BO.

### 2. Particle swarm optimization

Particle-swarm optimization (PSO) attempts to find the global maximum to an objective function by adjusting the trajectories of  $N_{\text{PSO}}$  individual particles. Each particle is described by a position vector  $\mathbf{x}_i$  whose components correspond

to one of the optimization parameters  $\theta, q_\beta, \xi$  and  $d$ . The particles are either distributed randomly or initialized on a grid in the landscape of optimization parameters. Additionally to the position vector, each particle is attributed with a velocity vector  $\mathbf{v}_i$  that iteratively updates the particle's position.

In standard PSO, the movement of particles depend on a stochastic and a deterministic component reflecting the trade-off between exploration and exploitation. To move from a current position at iteration step  $t$  to a next position at iteration step  $t + 1$ , each particle is attracted to the global best particle  $\mathbf{g}^*$  and its own best location  $\mathbf{x}_i^*$  in its past trajectory, while the full update also contains random numbers  $\varepsilon_1 \in (0, 1)$  and  $\varepsilon_2 \in (0, 1)$ . Introducing the learning parameters  $\alpha$  and  $\beta$ , the velocity and position at iteration step  $t + 1$  follow from the equations [89]

$$\mathbf{v}_i^{t+1} = \Omega_t \mathbf{v}_i^t + \alpha \varepsilon_1 (\mathbf{g}^* - \mathbf{x}_i^t) + \beta \varepsilon_2 (\mathbf{x}_i^* - \mathbf{x}_i^t) \quad (\text{A1})$$

$$\mathbf{x}_i^{t+1} = \mathbf{x}_i^t + \mathbf{v}_i^t. \quad (\text{A2})$$

where  $\Omega_t \in (0, 1)$  is called the inertia function. In each iteration step, we update the global best particle  $\mathbf{g}^*$  and the best location in the history of each particle  $\mathbf{x}_i^*$ . Additionally, we ensure that the particle's positions stay within the boundaries of the optimization parameter. The PSO algorithm terminates when a predefined number of iterations  $N_{\text{iter}}$  have been executed. The number  $N_{\text{iter}}$  was empirically determined by running the simulation a few times for the same values, and observing that the maximum of the objective function converged to the same value with same parameters. After every run, we checked that most of the particles ended in the same position. We set the default value of  $N_{\text{iter}}$  to  $10^3$ .

GPUs allow for a massively parallel implementation of the PSO algorithm. In our implementation, we addressed each particle  $\mathbf{x}_i$  to a single thread on the GPU, such that a maximal number of  $N_{\text{PSO}} = 10^8$  particles can search in parallel for the optimal optimization parameters. The optimal fidelities and parameters in Fig. 6 and Table III were computed with  $N_{\text{iter}} = 10^2$ ,  $\alpha = 0.05$  and  $\beta = 1.05$ , and we set the inertia function to  $\Omega_t = 0.5$ .

## Appendix B: Optimal parameters for the deterministic conversion protocol

In this Appendix we provide the result of the optimizations for the Gaussian maps corresponding to our deterministic conversion protocol introduced in Sec. III, in terms of the optimal parameters, that maximize the fidelity to the target state.

### 1. Symplectic Transformation

Here we show the symplectic transformations  $X$  that stem out of our optimization and yield the maximal values of the fidelity in Table I of the main text. The subindices correspond to the triplicity of the input trisqueezed state:

$$X_{0.1} = \begin{pmatrix} 1.2324 & 2 \cdot 10^{-7} \\ -4 \cdot 10^{-6} & 0.8114 \end{pmatrix},$$

$$X_{0.125} = \begin{pmatrix} 1.0002 & 4 \cdot 10^{-8} \\ 4 \cdot 10^{-7} & 0.9998 \end{pmatrix},$$

$$X_{0.15} = \begin{pmatrix} 0.7976 & -1 \cdot 10^{-6} \\ -5 \cdot 10^{-6} & 1.2538 \end{pmatrix}.$$

## Appendix C: Analytical derivations of the output state in the probabilistic protocol

In this Appendix, we present the analytical derivation of the output state corresponding to the probabilistic protocol sketched in Fig. 4.

The input state of this protocol is:

$$|\Psi_{\text{in}}\rangle |\Psi_{\xi, \beta}\rangle = \int dq_1 dq_2 \Psi_{\text{in}}(q_1) \Psi_{\xi, \beta}(q_2) |q_1, q_2\rangle. \quad (\text{C1})$$

After the real-valued beam-splitter transformation  $U_{BS}^R(2\theta)$ , we have

$$\begin{aligned} \Psi_{12}(\xi, \beta, \theta)\rangle &= U_{BS}^R(2\theta) |\Psi_{\text{in}}\rangle |\Psi_{\xi, \beta}\rangle \\ &= \int dq_1 dq_2 \Psi_{\text{in}}(q_1) \Psi_{\xi, \beta}(q_2) |q'_1\rangle |q'_2\rangle, \end{aligned} \quad (\text{C2})$$

where

$$|q'_1\rangle = |q_1 \cos \theta - q_2 \sin \theta\rangle, \quad (\text{C3})$$

$$|q'_2\rangle = |q_1 \sin \theta + q_2 \cos \theta\rangle. \quad (\text{C4})$$

Indicating with  $J(q'_1, q'_2)$  the Jacobian of the transformation, we have

$$\int dq_1 dq_2 F(q_1, q_2) = \int dq'_1 dq'_2 |J(q'_1, q'_2)| F(q'_1, q'_2), \quad (\text{C5})$$

where with a slight abuse of notation  $F(q'_1, q'_2) = F((q_1(q'_1, q'_2), (q_2(q'_1, q'_2)))$ . Here we have:

$$|J(q'_1, q'_2)| = \begin{vmatrix} \frac{\partial q_1}{\partial q'_1} & \frac{\partial q_1}{\partial q'_2} \\ \frac{\partial q_2}{\partial q'_1} & \frac{\partial q_2}{\partial q'_2} \end{vmatrix} = \begin{vmatrix} \cos \theta & \sin \theta \\ -\sin \theta & \cos \theta \end{vmatrix} = 1.$$

Hence, we can rewrite the state in Eq.(C2) as:

$$\begin{aligned} |\Psi_{12}(\xi, \beta, \theta)\rangle &= \int dq_1 dq_2 \Psi_{\text{in}}(q_1 \cos \theta + q_2 \sin \theta) \\ &\quad \Psi_{\xi, \beta}(-q_1 \sin \theta + q_2 \cos \theta) |q_1\rangle |q_2\rangle, \end{aligned} \quad (\text{C6})$$

where we have renamed  $q'_1 \rightarrow q_1$ ,  $q'_2 \rightarrow q_2$ .

Triplicity	Cubicity(5dB)	$X_{11}$	$X_{12}$	$X_{21}$	$X_{22}$	$Y_{11}$	$Y_{12}$	$Y_{22}$	$l_1$	$l_2$
0.1	0.1558	1.4837	0.0004	-0.0004	0.67400	$2 \cdot 10^{-7}$	$-3 \cdot 10^{-10}$	$8 \cdot 10^{-8}$	$-9 \cdot 10^{-5}$	0.15865
0.125	0.2757	1.2786	0.0003	-0.0001	0.7821	$8 \cdot 10^{-7}$	$1 \cdot 10^{-7}$	$3 \cdot 10^{-7}$	0.0001	0.2275
0.15	0.4946	1.0570	-0.0005	-0.0004	0.9461	$3 \cdot 10^{-7}$	$-7 \cdot 10^{-8}$	$4 \cdot 10^{-8}$	-0.0002	0.3031

TABLE VI: Optimized parameters for different triplicity, cubicity pairs for the Gaussian CP map.

After the phase rotation  $U_p(\gamma)$  on state  $|\Psi_{12}(\xi, \beta, \theta)\rangle$ , using the closure relation  $(1/\pi) \int |\alpha\rangle\langle\alpha| d\alpha^2 = I$  we obtain the state:

$$\begin{aligned} & U_p(\gamma) |\Psi_{12}(\xi, \beta, \theta)\rangle \\ &= \frac{1}{\pi} \int dq_1 dq_2 d\alpha \Psi_{\text{in}}(q_1 \cos \theta + q_2 \sin \theta) \\ & \quad \Psi_{\xi, \beta}(-q_1 \sin \theta + q_2 \cos \theta) \langle \alpha | q_2 \rangle |q_1\rangle |\alpha e^{-i\gamma}\rangle \\ & \equiv |\Psi_{12}(\xi, \beta, \theta, \gamma)\rangle, \end{aligned} \quad (\text{C7})$$

where

$$\langle \alpha | q_2 \rangle = \left( \frac{2}{\pi} \right)^{1/4} e^{iab} e^{-2ibq_2} e^{-(q_2-a)^2}, \quad (\text{C8})$$

and  $\alpha = a + ib$ .

When we measure  $\hat{q}$  on the 1<sup>st</sup> mode with the outcome  $q$ , we obtain on the second mode:

$$\begin{aligned} & |\Psi_{\text{out}}^q\rangle \\ &= \langle q | \Psi_{12}(\xi, \beta, \theta, \gamma)\rangle \\ &= \frac{1}{\pi} \int dq_2 d\alpha \Psi_{\text{in}}(q \cos \theta + q_2 \sin \theta) \\ & \quad \Psi_{\xi, \beta}(-q \sin \theta + q_2 \cos \theta) \langle \alpha | q_2 \rangle |\alpha e^{-i\gamma}\rangle. \end{aligned} \quad (\text{C9})$$

We now introduce the finitely resolved homodyne operator [101, 102]

$$\hat{Q}_n = \int_{q_n-\eta}^{q_n+\eta} dq |q\rangle\langle q|. \quad (\text{C10})$$

The density operator  $\hat{\rho}_{n, \text{cond}}$  on mode 2 conditioned on the measurement outcome  $q_n$  on mode 1 can be expressed in terms of (C9) and is given by

$$\begin{aligned} & \hat{\rho}_{n, \text{cond}} \\ &= \frac{\text{Tr}_1[\hat{Q}_n \otimes I_2 |\Psi_{12}(\xi, \beta, \theta, \gamma)\rangle\langle \Psi_{12}(\xi, \beta, \theta, \gamma)| \hat{Q}_n \otimes I_2]}{\text{Prob}[q_n]} \\ &= \frac{\int_{q_n-\eta}^{q_n+\eta} dq \langle q | \Psi_{12}(\xi, \beta, \theta, \gamma)\rangle\langle \Psi_{12}(\xi, \beta, \theta, \gamma)| q \rangle_1}{\text{Prob}[q_n]} \\ &= \frac{1}{\text{Prob}[q_n]} \int_{q_n-\eta}^{q_n+\eta} dq |\Psi_{\text{out}}^q\rangle\langle \Psi_{\text{out}}^q|, \end{aligned} \quad (\text{C11})$$

where  $\text{Tr}_1$  is the partial trace over mode 1, and the probability

of obtaining an outcome  $q_n$  is expressed as:

$$\begin{aligned} & \text{Prob}[q_n] \\ &= \langle \Psi_{12}(\xi, \beta, \theta, \gamma) | \hat{Q}_n \otimes I_2 | \Psi_{12}(\xi, \beta, \theta, \gamma) \rangle \\ &= \int_{q_n-\eta}^{q_n+\eta} dq \langle \Psi_{12}(\xi, \beta, \theta, \gamma) | q \rangle\langle q | \Psi_{12}(\xi, \beta, \theta, \gamma) \rangle \\ &= \frac{1}{\pi^2} \int_{q_n-\eta}^{q_n+\eta} dq \int dq_2 dq'_2 d\alpha d\alpha' \Psi_{\text{in}}^*(q \cos \theta + q'_2 \sin \theta) \\ & \quad \Psi_{\text{in}}(q \cos \theta + q_2 \sin \theta) \Psi_{\xi, \beta}(q_2 \cos \theta - q \sin \theta) \\ & \quad \Psi_{\xi, \beta}^*(q'_2 \cos \theta - q \sin \theta) \langle q'_2 | \alpha' \rangle\langle \alpha | q_2 \rangle\langle \alpha' | \alpha \rangle \\ &= \int_{q_n-\eta}^{q_n+\eta} dq \int dq_2 |\Psi_{\text{in}}(q \cos \theta + q_2 \sin \theta)|^2 \\ & \quad |\Psi_{\xi, \beta}(q_2 \cos \theta - q \sin \theta)|^2, \end{aligned} \quad (\text{C12})$$

where we have used that

$$\begin{aligned} & \int d\alpha d\alpha' \langle q'_2 | \alpha' \rangle\langle \alpha | q_2 \rangle\langle \alpha' | \alpha \rangle \\ &= \int d\alpha d\alpha' \left( \frac{2}{\pi} \right)^{1/2} e^{iab} e^{-2ibq_2} e^{-(q_2-a)^2} \\ & \quad e^{-ia'b'} e^{2ib'q'_2} e^{-(q'_2-a')^2} \\ & \quad \exp \left\{ -\frac{|\alpha'|^2}{2} - \frac{|\alpha|^2}{2} + \alpha'^* \alpha \right\} \\ &= \pi^2 e^{-\frac{1}{2}(q_2-q'_2)^2} \delta(q_2-q'_2). \end{aligned} \quad (\text{C13})$$

Our fidelity can be written as

$$\begin{aligned} F_{q_n} &= \langle \Psi_{\text{target}} | \hat{\rho}_{n, \text{cond}} | \Psi_{\text{target}} \rangle \\ &= \frac{1}{\text{Prob}[q_n]} \int_{q_n-\eta}^{q_n+\eta} dq |\langle \Psi_{\text{target}} | \Psi_{\text{out}}^q \rangle|^2, \end{aligned} \quad (\text{C14})$$

where the output state is given in Eq.(D1). We can write the overlap as:

$$\begin{aligned} & \langle \Psi_{\text{target}} | \Psi_{\text{out}}^q \rangle \\ &= \frac{1}{\pi} \int dq_0 dq_2 d\alpha \Psi_{\text{target}}^*(q_0) \Psi_{\text{in}}(q \cos \theta + q_2 \sin \theta) \\ & \quad \Psi_{\xi, \beta}(-q \sin \theta + q_2 \cos \theta) \langle q_2 | \alpha \rangle^* \langle q_0 | \alpha e^{-i\gamma} \rangle, \end{aligned} \quad (\text{C15})$$

where

$$\begin{aligned} & \int d\alpha \langle q_2 | \alpha \rangle^* \langle q_0 | \alpha e^{-i\gamma} \rangle \\ &= \sqrt{\frac{2}{\pi}} \frac{1}{\sqrt{1-e^{-2i\gamma}}} \\ & \quad \exp(i \csc \gamma (-2q_0 q_2 + (q_0^2 + q_2^2) \cos \gamma)). (\gamma \neq 0) \end{aligned} \quad (\text{C16})$$

Finally, we obtain the expression for the fidelity by combining Eq.(C11), Eq.(C15) and Eq.(C16):

$$F_{q_n}(q_n, \eta, \gamma, \theta, \xi, \beta) = \frac{\int_{q_n-\eta}^{q_n+\eta} dq |\langle \Psi_{\text{target}} | \Psi_{\text{out}}^q \rangle|^2}{\text{Prob}[q_n]}, \quad (\text{C17})$$

where we have explicated the dependence on the squeezed state parameters, and where

$$\begin{aligned} & \int_{q_n-\eta}^{q_n+\eta} dq |\langle \Psi_{\text{target}} | \Psi_{\text{out}}^q \rangle|^2 \\ &= \int_{q_n-\eta}^{q_n+\eta} dq \left| \int dq_0 dq_2 \Psi_{\text{target}}^*(q_0) \Psi_{\text{in}}(q \cos \theta + q_2 \sin \theta) \right. \\ & \quad \left. \Psi_{\xi, \beta}(-q \sin \theta + q_2 \cos \theta) \right. \\ & \quad \left. \sqrt{\frac{2}{\pi}} e^{i \csc \gamma (-2q_0 q_2 + (q_0^2 + q_2^2) \cos \gamma)} / \sqrt{1 - e^{-2i\gamma}} \right|^2. \end{aligned} \quad (\text{C18})$$

#### Appendix D: Which parameters control which property of the output state?

The symmetry of the Wigner function plays an important role in this optimization problem, and has a lot of applications, for instance in the design of rotationally-symmetric bosonic codes [103]. We now discuss, relative to the second protocol that we have introduced, the relationship between the tunable parameters of our protocol and the Wigner function of the output state.

Fig. 8 shows that the amount of negativity in the output state increases with increasing  $\theta$ . This happens because  $\cos \theta$  and  $\sin \theta$  are the transmission and reflection coefficients of the beam-splitter, respectively. If the trisqueezed state is mostly reflected, then it is expected that the negativity in the output will be negligible. The cubicity in the output state on the lower rail, therefore, will be proportional to  $\sin \theta$ .

Another important property can be revealed by Fig. 9. The Wigner negativity is changed when varying the displacement parameter of the input squeezed state: it is becomes higher when the squeezed state is displaced further from the original point in the position direction. Similarly, the direction of the squeezing in the ancillary squeezed state,  $\text{Arg}(\xi)$ , affects the main negative curves. The width of the Wigner function is instead influenced by the strength of the parameter  $\xi$ .

#### Appendix E: Interpretation of the probabilistic protocol

In this appendix, we aim at showing that the effect of the probabilistic protocol is to introduce squeezing on the input state, in line with the findings of Sec.III B. For simplicity, we ignore the final phase rotation and the output state can thus be written as Eq .D1. where  $c_1 = \sin \theta$ ,  $c_2 = \cos \theta$ ,  $b_1 = q \cos \theta$ ,  $b_2 = -q \sin \theta$ ,  $-e^{2\xi_1} = c_2$ , and  $\Psi_{\xi, \beta}(c_2 q_2 + b_2)$  is a Gaussian filter [33, 39]. Note that for  $q = 0$  we obtain a zero

displacement. This situation is reminiscent of gate teleportation.

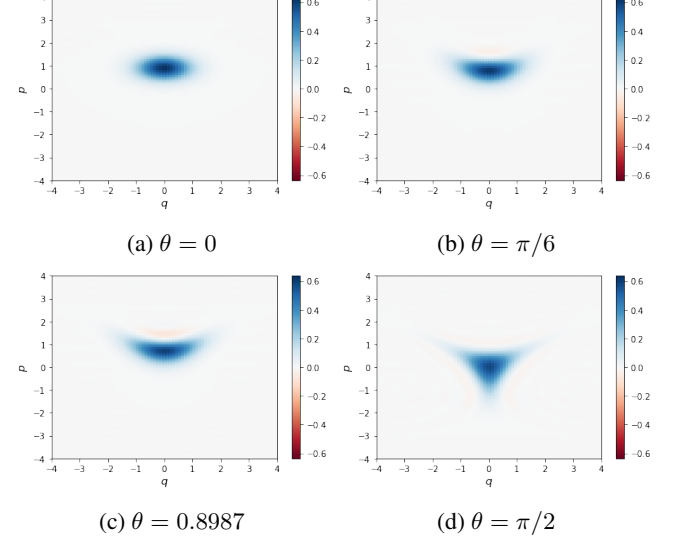


FIG. 8: Wigner function of the output state while changing  $\theta$  from 0 degree to 90 degree. The other parameters are shown in the first row of Table. III. Notice that Fig. 8c corresponds to the optimal result.

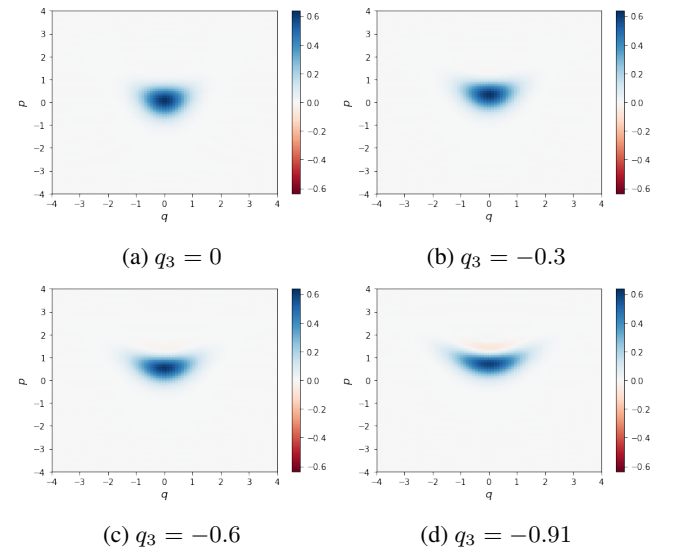


FIG. 9: The Wigner function of the output states while changing the parameter  $q_3$ , corresponding to the displacement in position of the input ancillary squeezed state. We fix other parameters as shown in the first row of Table. III. Also notice that Fig. 9d corresponds to the optimal result.

Under the conditions in which the filtering factor tends to 1, we expect therefore the probabilistic protocol to tend to the deterministic protocol. Note that, as we have said in Sec. III B, the latter yields fidelity of conversion 1 when the optimal squeezing for the conversion tends to infinity.

$$\begin{aligned}
|\Psi_{\text{out}}^q\rangle &= \langle q|\Psi_{12}(\xi, \beta, \theta, \gamma)\rangle \\
&= \int dq_2 \Psi_{\xi, \beta}(-q \sin \theta + q_2 \cos \theta) \Psi_{\text{in}}(q \cos \theta + q_2 \sin \theta) |q_2\rangle \\
&= \int dq_2 \Psi_{\xi, \beta}(b_2 + c_2 q_2) \Psi_{\text{in}}(b_1 + c_1 q_2) |q_2\rangle \\
&= \Psi_{\xi, \beta}(c_2 \hat{q}_2 + b_2) \int dq_2 \Psi_{\text{in}}(c_1(q_2 + \frac{b_1}{c_1})) |q_2\rangle \\
&= \Psi_{\xi, \beta}(c_2 \hat{q}_2 + b_2) \hat{D}\left(\frac{b_1}{c_1}\right) \hat{S}(\xi_1) \int dq_2 \Psi_{\text{in}}(q_2) |q_2\rangle \\
&= \Psi_{\xi, \beta}(c_2 \hat{q}_2 + b_2) \hat{D}\left(\frac{b_1}{c_1}\right) \hat{S}(\xi_1) |\Psi_{\text{in}}\rangle
\end{aligned} \tag{D1}$$

---

[1] A. Serafini, *Quantum Continuous Variables: A Primer of Theoretical Methods* (CRC press, 2017).

[2] O. Pfister, Journal of Physics B: Atomic, Molecular and Optical Physics **53**, 012001 (2019).

[3] A. Blais, A. L. Grimsmo, S. Girvin, and A. Wallraff, arXiv preprint arXiv:2005.12667 (2020).

[4] A. L. Grimsmo and A. Blais, npj Quantum Information **3**, 1 (2017).

[5] T. Hillmann, F. Quijandra, G. Johansson, A. Ferraro, S. Gasparinetti, and G. Ferrini, arXiv:2002.01402 [quant-ph].

[6] A. Serafini, A. Retzker, and M. B. Plenio, New Journal of Physics **11**, 023007 (2009).

[7] C. Flühmann, T. L. Nguyen, M. Marinelli, V. Negnevitsky, K. Mehta, and J. P. Home, Nature **566**, 513 (2019).

[8] M. Schmidt, M. Ludwig, and F. Marquardt, New Journal of Physics **14**, 125005 (2012).

[9] O. Houhou, H. Aissaoui, and A. Ferraro, Physical Review A **92**, 063843 (2015).

[10] W. H. P. Nielsen, Y. Tsaturyan, C. B. Møller, E. S. Polzik, and A. Schliesser, Proceedings of the National Academy of Sciences **114**, 62 (2017).

[11] J. Stasińska, C. Rodó, S. Paganelli, G. Birkl, and A. Sanpera, Physical Review A **80**, 062304 (2009).

[12] D. F. Milne and N. V. Korolkova, Physical Review A **85**, 032310 (2012).

[13] Y. Ikeda and N. Yamamoto, Physical Review A **87**, 033802 (2013).

[14] K. R. Motes, B. Q. Baragiola, A. Gilchrist, and N. C. Menicucci, Physical Review A **95**, 053819 (2017).

[15] L. Aolita, A. J. Roncaglia, A. Ferraro, and A. Acín, Physical Review Letters **106**, 090501 (2011).

[16] J. Yoshikawa, S. Yokoyama, T. Kaji, C. Sornphiphatphong, Y. Shiozawa, K. Makino, and A. Furusawa, APL Photonics **1**, 060801 (2016).

[17] M. V. Larsen, X. Guo, C. R. Breum, J. S. Neergaard-Nielsen, and U. L. Andersen, Science **366**, 369 (2019).

[18] W. Asavanant, Y. Shiozawa, S. Yokoyama, B. Charoensombutamon, H. Emura, R. N. Alexander, S. Takeda, J.-i. Yoshikawa, N. C. Menicucci, H. Yonezawa, *et al.*, Science **366**, 373 (2019).

[19] F. Lenzini, J. Janousek, O. Thearle, M. Villa, B. Haylock, S. Kasture, L. Cui, H.-P. Phan, D. V. Dao, H. Yonezawa, *et al.*, Science advances **4**, eaat9331 (2018).

[20] N. Ofek, A. Petrenko, R. Heeres, P. Reinhold, Z. Leghtas, B. Vlastakis, Y. Liu, L. Frunzio, S. M. Girvin, L. Jiang, M. Mirrahimi, M. H. Devoret, and R. J. Schoelkopf, Nature **536**, 441 (2016).

[21] A. Romanenko, R. Pilipenko, S. Zorzetti, D. Frolov, M. Awida, S. Belomestnykh, S. Posen, and A. Grassellino, Physical Review Applied **13**, 034032 (2020).

[22] D. Gottesman, A. Kitaev, and J. Preskill, Physical Review A **64**, 012310 (2001).

[23] N. C. Menicucci, Phys. Rev. Lett. **112**, 120504 (2014).

[24] P. Campagne-Ibarcq, A. Eickbusch, S. Touzard, E. Zalys-Geller, N. Frattini, V. Sivak, P. Reinhold, S. Puri, S. Shankar, R. Schoelkopf, *et al.*, arXiv:1907.12487 (2019).

[25] A. Ferraro, S. Olivares, and M. G. A. Paris, *Gaussian States in Quantum Information* (Bibliopolis, Napoli, 2005).

[26] C. Weedbrook, S. Pirandola, R. García-Patrón, N. J. Cerf, T. C. Ralph, J. H. Shapiro, and S. Lloyd, Rev. Mod. Phys. **84**, 621 (2012).

[27] G. Adesso, S. Ragy, and A. R. Lee, Open Systems & Information Dynamics **21**, 1440001 (2014).

[28] S. Lloyd and S. L. Braunstein, in *Quantum Information with Continuous Variables* (Springer, 1999) pp. 9–17.

[29] F. Albarelli, M. G. Genoni, M. G. Paris, and A. Ferraro, Physical Review A **98**, 052350 (2018).

[30] R. Takagi and Q. Zhuang, Physical Review A **97**, 062337 (2018).

[31] B. Q. Baragiola, G. Pantaleoni, R. N. Alexander, A. Karanjai, and N. C. Menicucci, Phys. Rev. Lett. **123**, 200502 (2019).

[32] H. Yamasaki, T. Matsuura, and M. Koashi, Physical Review Research **2**, 023270 (2020).

[33] M. Gu, C. Weedbrook, N. C. Menicucci, T. C. Ralph, and P. van Loock, Phys. Rev. A **79**, 062318 (2009).

[34] T. Douce, D. Markham, E. Kashefi, P. van Loock, and G. Ferrini, Physical Review A **99**, 012344 (2019).

[35] C. Flühmann, V. Negnevitsky, M. Marinelli, and J. P. Home, Phys. Rev. X **8**, 021001 (2018).

[36] S. Ghose and B. C. Sanders, J. Mod. Opt. **54**, 855 (2007).

[37] K. Miyata, H. Ogawa, P. Marek, R. Filip, H. Yonezawa, J.-i. Yoshikawa, and A. Furusawa, Phys. Rev. A **93**, 233602 (2016).

[38] F. Arzani, N. Treps, and G. Ferrini, Phys. Rev. A **95**, 052352 (2017).

[39] K. K. Sabapathy, H. Qi, J. Izaac, and C. Weedbrook, Physical Review A **100**, 012326 (2019).

[40] R. Yanagimoto, T. Onodera, E. Ng, L. G. Wright, P. L. McMa-

hon, and H. Mabuchi, *Physical Review Letters* (2020).

[41] M. Yukawa, K. Miyata, H. Yonezawa, P. Marek, R. Filip, and A. Furusawa, *Phys. Rev. A* **88**, 053816 (2013).

[42] M. Dakna, T. Anhut, T. Opatrný, L. Knöll, and D.-G. Welsch, *Physical Review A* **55**, 3184 (1997).

[43] J. Wenger, R. Tualle-Brouri, and P. Grangier, *Phys. Rev. Lett.* **92**, 153601 (2004).

[44] V. Parigi, A. Zavatta, M. Kim, and M. Bellini, *Science* **317**, 1890 (2007).

[45] M. Hofheinz, E. Weig, M. Ansmann, R. C. Bialczak, E. Lucero, M. Neeley, A. OConnell, H. Wang, J. M. Martinis, and A. Cleland, *Nature* **454**, 310 (2008).

[46] R. W. Heeres, B. Vlastakis, E. Holland, S. Krastanov, V. V. Albert, L. Frunzio, L. Jiang, and R. J. Schoelkopf, *Phys. Rev. Lett.* **115**, 137002 (2015).

[47] G. Kirchmair, B. Vlastakis, Z. Leghtas, S. E. Nigg, H. Paik, E. Ginossar, M. Mirrahimi, L. Frunzio, S. M. Girvin, and R. J. Schoelkopf, *Nature (London)* **495**, 205 (2013).

[48] I.-M. Svensson, A. Bengtsson, J. Bylander, V. Shumeiko, and P. Delsing, *Applied Physics Letters* **113**, 022602 (2018).

[49] S. Touzard, A. Grimm, Z. Leghtas, S. O. Mundhada, P. Reinhold, C. Axline, M. Reagor, K. Chou, J. Blumoff, K. M. Sliwa, S. Shankar, L. Frunzio, R. J. Schoelkopf, M. Mirrahimi, and M. H. Devoret, *Phys. Rev. X* **8**, 021005 (2018).

[50] A. Grimm, N. E. Frattini, S. Puri, S. O. Mundhada, S. Touzard, M. Mirrahimi, S. M. Girvin, S. Shankar, and M. H. Devoret, *arXiv e-prints* (2019), arXiv:1907.12131 [quant-ph].

[51] C. W. S. Chang, C. Sabín, P. Forn-Díaz, F. Quijandría, A. M. Vadiraj, I. Nsanzineza, G. Johansson, and C. M. Wilson, *Phys. Rev. X* **10**, 011011 (2020).

[52] R. Lescanne, M. Villiers, T. Peronnin, A. Sarlette, M. Delbecq, B. Huard, T. Kontos, M. Mirrahimi, and Z. Leghtas, *Nature Physics* **16**, 509 (2020).

[53] V. V. Donodov and V. I. Mank'o, *Theory of Nonclassical states of light* (CRC Press, 2003).

[54] U. Leonhardt, *Essential Quantum Optics: from Quantum Measurements to Black Holes* (Cambridge University Press, 2010).

[55] S. L. Braunstein and R. McLachlan, in *Journal of the Optical Society of America A-Optics Image Science and Vision*, Vol. 3 (1986) pp. P46–P46.

[56] K. Banaszek and P. L. Knight, *Physical Review A* **55**, 2368 (1997).

[57] V. V. Albert and L. Jiang, *Physical Review A* **89**, 022118 (2014).

[58] Note that the value of the cubicity depends on the convention used. In our case, the values refer to  $\hbar = 1/2$ .

[59] A. Mari and J. Eisert, *Physical Review Letters* **109**, 230503 (2012).

[60] K. E. Cahill and R. J. Glauber, *Phys. Rev.* **177**, 1857 (1969).

[61] G. De Palma, A. Mari, V. Giovannetti, and A. S. Holevo, **56**, 052202.

[62] F. M. Dopico and C. R. Johnson, **31**, 650.

[63] K. E. Cahill and R. J. Glauber, *Physical Review* **177**, 1882 (1969).

[64] M. A. Nielsen and I. L. Chuang, *Physical Review Letters* **79**, 321 (1997).

[65] D. Gottesman and I. L. Chuang, *Nature* **402**, 390 (1999).

[66] S. D. Bartlett and W. J. Munro, *Physical Review Letters* **90**, 117901 (2003).

[67] NVIDIA Corporation, “NVIDIA CUDA C programming guide,” (2019), version 10.2.

[68] D. Matthews, *Nature* **562**, 151 (2018).

[69] M. H. Devoret and J. M. Martinis, *Quantum Inf. Process.* **3**, 163203 (2004).

[70] X. Gu, A. F. Kockum, A. Miranowicz, Y. xi Liu, and F. Nori, *Physics Reports* **718-719**, 1 (2017), microwave photonics with superconducting quantum circuits.

[71] W. Wustmann and V. Shumeiko, *Phys. Rev. B* **87**, 184501 (2013).

[72] W. Wustmann and V. Shumeiko, *Phys. Rev. Applied* **8**, 024018 (2017).

[73] Y. Y. Gao, B. J. Lester, Y. Zhang, C. Wang, S. Rosenblum, L. Frunzio, L. Jiang, S. Girvin, and R. J. Schoelkopf, *Physical Review X* **8**, 021073 (2018).

[74] C. Eichler, D. Bozyigit, and A. Wallraff, *Phys. Rev. A* **86**, 032106 (2012).

[75] T. Walter, P. Kurpiers, S. Gasparinetti, P. Magnard, A. Potočnik, Y. Salathé, M. Pechal, M. Mondal, M. Oppliger, C. Eichler, *et al.*, *Physical Review Applied* **7**, 054020 (2017).

[76] W. Pfaff, C. J. Axline, L. D. Burkhardt, U. Vool, P. Reinhold, L. Frunzio, L. Jiang, M. H. Devoret, and R. J. Schoelkopf, *Nature Physics* **13**, 882 (2017).

[77] H. Vahlbruch, M. Mehmet, K. Danzmann, and R. Schnabel, *Physical Review Letters* **117**, 110801 (2016).

[78] Y. Cai, J. Roslund, G. Ferrini, F. Arzani, X. Xu, C. Fabre, and N. Treps, *Nature Communications* **8**, 15645 (2017).

[79] E. R. González, A. Borne, B. Boulanger, J. Levenson, and K. Bencheikh, *Physical Review Letters* **120**, 043601 (2018).

[80] C. Okoth, A. Cavanna, N. Y. Joly, and M. V. Chekhova, *Physical Review A* **99**, 043809 (2019).

[81] J. Nickolls, I. Buck, M. Garland, and K. Skadron, *Queue* **6**, 4053 (2008).

[82] The GPyOpt authors, “GPyOpt: A bayesian optimization framework in python,” <http://github.com/SheffieldML/GPyOpt> (2016).

[83] H. J. Kushner, *Journal of Fluids Engineering, Transactions of the ASME* **86(1)**, 97 (1964).

[84] J. Mockus, Springer, Dordrecht (1989).

[85] N. Bell and J. Hoberock, in *GPU Computing Gems Jade Edition*, Applications of GPU Computing Series, edited by W. mei W. Hwu (Morgan Kaufmann, Boston, 2012) pp. 359 – 371.

[86] K. Kaczmarski and P. Rzkażewski, in *New Trends in Databases and Information Systems*, edited by M. Pechenizkiy and M. Wojciechowski (Springer Berlin Heidelberg, Berlin, Heidelberg, 2013) pp. 37–46.

[87] E. Wynters, *J. Comput. Sci. Coll.* **28**, 148155 (2013).

[88] J. Kennedy and R. Eberhart, *Proceedings of ICNN’95 - International Conference on Neural Networks* **4**, 1942 (1995).

[89] X.-S. Yang, S. Deb, and S. Fong, In: Fong S. (eds) *Networked Digital Technologies. Communications in Computer and Information Science*, vol 136. Springer, Berlin, Heidelberg (2011).

[90] J. Johansson, P. Nation, and F. Nori, *Computer Physics Communications* **183**, 1760 (2012).

[91] J. Johansson, P. Nation, and F. Nori, *Computer Physics Communications* **184**, 1234 (2013).

[92] C. G. BROYDEN, *IMA Journal of Applied Mathematics* **6**, 76 (1970).

[93] R. Fletcher, *The Computer Journal* **13**, 317 (1970).

[94] D. F. Shanno, *Mathematics of Computation* **24**, 647 (1970).

[95] D. Goldfarb, *Mathematics of Computation* **24**, 23 (1970).

[96] C. Sanderson and R. Curtin, *The Journal of Open Source Software* **1**, 26 (2016).

[97] C. Sanderson and R. Curtin, “A User-Friendly Hybrid Sparse Matrix Class in C++,” e-print arXiv:1805.03380 (2018).

[98] K. O’Hara, “Optimlib,” <https://github.com/kthohr/optim> (2020).

- [99] R. Storn and K. Price, *J. of Global Optimization* **11**, 341359 (1997).
- [100] A. Ekström, C. Forssn, C. Dimitrakakis, D. Dubhashi, H. T. Johansson, A. S. Muhammad, H. Salomonsson, and A. Schliep, *J. Phys. G: Nucl. Part. Phys.* **46**, 095101 (2019).
- [101] M. G. A. Paris, M. Cola, and R. Bonifacio, *Phys. Rev. A* **67**, 042104 (2003).
- [102] T. Douce, D. Markham, E. Kashefi, E. Diamanti, T. Coudreau, P. Milman, P. van Loock, and G. Ferrini, *Physical Review Letters* **118**, 070503 (2017).
- [103] B. B. Q. Grimsmo A L, Combes J, *Physical Review X* **10**(1), 011058 (2020).